Desalination and Water Treatment
www.deswater.com

doi: 10.5004/dwt.2022.28894

276 (2022) 224–236
November

Synthesis of Ag_3VO_4/Bi_2WO_6 heterojunction photocatalyst with enhanced photocatalytic activity under visible light irradiation by hydrothermal methods

Chung-Hsin Wu*, Syuan-Ru Jhu

Department of Chemical and Materials Engineering, National Kaohsiung University of Science and Technology, 415 Chien Kung Road, Kaohsiung, Taiwan, Tel. 886-7-3814526; Fax: 886-7-3830674; email: wuch@nkust.edu.tw (C.-H. Wu), Tel. 886-7-3814526; email: f107146119@nkust.edu.tw (S.-R. Jhu)

Received 3 July 2022; Accepted 4 September 2022

ABSTRACT

Ag_3VO_4 (AVO)/Bi_2WO_6 (BWO) composites with different AVO/BWO molar ratios were synthesized using a single-step hydrothermal method. The photocatalytic performance of the synthesized photocatalysts in the degradation of C.I. Reactive Red 2 (RR2) under visible light (Vis.) irradiation was evaluated. The AVO/BWO composites were characterized by X-ray diffraction analysis, scanning electron microscopy, transmission electron microscopy, ultraviolet-visible (UV-Vis) spectroscopy, photoluminescence spectroscopy, Brunauer–Emmett–Teller analysis and X-ray photoelectron spectroscopy. Scavenger experiments were performed to determine the photocatalytic mechanism. The AVO/BWO composites exhibited much greater photocatalytic efficiency than pure AVO and BWO; moreover, AVO/BWO molar ratio of 1/3 (AB3) yielded the best photo-activity. AB3 exhibited the greatest photocatalytic performance, with RR2 removal efficiencies of 82% and 92% under Vis. and solar irradiations, respectively. The RR2 photodegradation rate constant of AB3 was 0.0894 min^{-1}, which was about 13.5 and 16.9 times those of AVO and BWO under Vis. irradiation, respectively. The excellent photo-activity of AB3 is attributable to improved light absorption across the entire spectrum, its large specific surface area, the separation of photo-generated electron–hole pairs, and a synergetic interaction between AVO and BWO. Additionally, the photo-stability of AB3 was greater than that of AVO. The scavenger experimental results suggested that photocatalytic RR2 degradation over AB3 was mainly governed by direct photo-generated hole oxidation.

Keywords: Ag_3VO_4; Bi_2WO_6; Hydrothermal; Heterojunction; Visible light; Photodegradation

1. Introduction

The various methods for removing organic pollutants from wastewater include adsorption [1], microwave catalysis [2] and photocatalysis [3,4]. Adsorption is an effective and cheap method for removing pollutants from wastewater, but they only change their phase from solute to solid: they do not degrade them. Microwave-induced catalytic oxidation is favorable owing to its short reaction time, low energy consumption and excellent degradation performance [2]. However, the required microwave equipment and consumed energy are expensive. Photocatalysis has the advantage of high oxidation efficiency. However, photocatalysis consumes energy and the generated intermediates may be more toxic than the parent compound. The low reagent utilization, high cost, secondary pollution and other disadvantages limit the application of these methods.

* Corresponding author.

Semiconductor photocatalysis is a cost-effective, renewable, and environmentally friendly technique for solar energy utilization and environmental remediation. Recently, attention has been increasingly focused on the use of photocatalysts for environmental purification and energy conservation. Researchers have devoted much effort to the fabrication of visible light (Vis.)-driven photocatalysts for use in the treatment of wastewater. The ideal photocatalyst should have a low band gap, high dispersibility, non-toxicity, resistance to photo-corrosion, and outstanding photo-activity in the degradation of pollutants under Vis. illumination.

Silver vanadate (Ag_3VO_4, AVO), which was first synthesized by Konta et al. [5], exhibits photo-activity in the evolution of O_2 from H_2O under Vis. irradiation and has therefore attracted considerable attention. However, AVO suffers from serious photo-corrosion and the recombination of photo-generated electrons (e^-) and holes (h^+) during photocatalysis. Combining AVO with low-cost semiconductors can reduce the cost of the prepared photocatalysts. In recent years, heterostructural composites of pairs of semiconductors have been recognized as promising in the development of highly efficient photocatalytic materials. The different band gap potentials in heterostructures can induce irreversible charge carrier separation and transfer at the interface, weakening recombination and promoting efficient electron–hole separation, increasing photo-activity [6,7].

Bismuth tungstate (Bi_2WO_6, BWO) is one of the simplest members of the Aurivillius oxide family and is a Vis.-responsive photocatalytic material; however, the rapid recombination of photo-generated electron–hole pairs seriously limits its efficiency of energy conversion. To increase the utilization rate of Vis. and to promote the separation of photo-induced e^- and h^+, the design of a heterojunction structure by coupling BWO with other photocatalyst with matching band potentials is feasible. The conduction band (CB) potential of BWO (0.275 eV) [8] exceeds that of AVO (0.25 eV) [9], and the valence band (VB) potential of BWO (3.125 eV) [8] exceeds that of AVO (2.05 eV) [9]. Accordingly, BWO is an ideal candidate to hybridize with AVO to form a staggered band gap type heterojunction, providing efficient separation and migration of photo-generated carriers and thus high photo-activity.

AVO can be combined with bismuth-based oxides such as $BiPO_4$ [10], BiOCl [11], BWO [12,13], BiOBr [14], BiOI [15], $BiOIO_3$ [16], Bi_2O_3 [17], $BiVO_4$ [18,19] and Bi_2O_3/$BiVO_4$ [20], forming heterojunctions, which improve photocatalytic performance by reducing the probability of recombination of the photo-generated e^- and h^+. Various methods have been used to prepare heterojunction materials; they include the hydrothermal process, sonochemical method, solvothermal process, solid-state reaction method, co-precipitation, sol–gel method, microwave synthesis and chemical deposition. Li et al. [12] and Zhang and Ma [13] synthesized AVO/BWO composites by growing AVO particles *in situ* onto BWO nanosheets by chemical deposition. Their heterojunction with an AVO/BWO molar ratio of 0.15/1 exhibited the highest photo-activity, which was 6.7 or 1.7 times greater than that of pure BWO or AVO [12]. Zhang and Ma [13] found that an AVO/BWO heterojunction with the optimal BWO/AVO mass ratio of 10% exhibited the highest photo-activity. Researchers have not yet used a single-step hydrothermal method to synthesize AVO/BWO composites with various AVO/BWO molar ratios and compared the photo-activities of such prepared AVO/BWO composites under Vis. irradiation. Their photo-activity is evaluated by using them in the photodegradation of C.I. Reactive Red 2 (RR2). The goals of the present study are (i) to synthesize AVO/BWO composites with different AVO/BWO molar ratios by the single-step hydrothermal method; (ii) to measure the surface characteristics and compare the photo-activity of the prepared AVO/BWO composites, (iii) to compare the photo-activity of AVO/BWO composite through single-step and two-step hydrothermal methods; (iv) to determine the reusability and the active reaction species of AVO/BWO composites at the optimal AVO/BWO molar ratio, and (v) to propose a mechanism of photo-activity of the AVO/BWO composites.

2. Materials and methods

2.1. Materials

All reagents were analytical-grade and used as received without further purification. Deionized water (DW) was used throughout this study. Silver nitrate ($AgNO_3$) and RR2 ($C_{19}H_{10}Cl_2N_6Na_2O_7S_2$) were obtained from Sigma-Aldrich (USA). Sodium orthovanadate (Na_3VO_4) was obtained from Alfa Aesar (USA). Bismuth(III) nitrate ($Bi(NO_3)_3{\cdot}5H_2O$), sodium tungstate ($Na_2WO_4{\cdot}2H_2O$), trisodium citrate ($Na_3C_6H_5O_7{\cdot}2H_2O$, TCD), NaOH, HNO_3, disodium ethylenediamine tetraacetate ($C_{10}H_{14}N_2O_8Na_2{\cdot}2H_2O$, EDTA-2Na) and potassium chromate (K_2CrO_4) were all purchased from Katayama (Japan). Isopropanol (IPA) was purchased from J.T. Baker (USA).

2.2. Procedures for synthesizing photocatalysts

2.2.1. Synthesis of AVO

A 2.5485 g mass of $AgNO_3$ and 1.0217 g of Na_3VO_4 were dissolved in 60 mL DW to yield solutions A and B, respectively. Solutions A, B and 0.4456 g TCD were mixed and adjusted to pH 7 by adding 10 M NaOH or HNO_3 and stirring (600 rpm) for 30 min. The adjusted mixture was sealed in a 200 mL Teflon-lined stainless autoclave and maintained at 393 K for 6 h; it was then left to cool naturally to room temperature. The precipitates thus obtained were collected by filtration and washed using 50 mL 95% ethanol and 100 mL DW to remove any residual impurities. The samples were finally dried in air at 333 K for 24 h to yield AVO.

2.2.2. Synthesis of BWO

A 3.881 g mass of $Bi(NO_3)_3{\cdot}5H_2O$ was dissolved in 60 mL HNO_3 (2 M) to yield solution C. A 1.319 g mass of $Na_2WO_4{\cdot}2H_2O$ was dissolved in 60 mL NaOH (2 M) to yield solution D. Solutions C and D were mixed and adjusted to pH 7 by adding 10 M NaOH or HNO_3 and stirring (600 rpm) for 30 min. The adjusted mixture was sealed in a 200 mL Teflon-lined stainless autoclave and maintained at 433 K for 12 h. The subsequent procedures and conditions that

were used to generate BWO were the same as those used to generate AVO.

2.2.3. Synthesis of AVO/BWO composites

Five AVO/BWO molar ratios (1/1, 1/2, 1/3, 1/4 and 2/1) were used in the syntheses, yielding AB1, AB2, AB3, AB4 and AB5. The AB1–AB5 composites were prepared by the single-step hydrothermal process. The details of the preparation of AB1 are as follows. A 1.2743 g mass of $AgNO_3$ and 0.5109 g of Na_3VO_4 were dissolved in 30 mL DW to yield solutions E and F, respectively. Solutions E, F and 0.4456 g TCD were mixed and adjusted to pH 7 by adding 10 M NaOH or HNO_3 and stirring (600 rpm) for 30 min, yielding the solution of AVO precursors. A 2.4254 g mass of $Bi(NO_3)_3{\cdot}5H_2O$ was dissolved in 30 mL HNO_3 (2 M) to yield solution G. A 0.8247 g mass of $Na_2WO_4{\cdot}2H_2O$ was dissolved in 30 mL NaOH (2 M) to yield solution H. Solutions G and H were mixed and adjusted to pH 7 by adding 10 M NaOH or HNO_3 and stirring (600 rpm) for 30 min, yielding the solution of BWO precursors. The solutions of AVO and BWO precursors were mixed and adjusted to pH 7 with stirring (600 rpm) for 30 min. This mixture was sealed in a 200 mL Teflon-lined stainless autoclave and maintained at 393 K for 6 h. The subsequent procedures and conditions that were used to generate AB1 were the same as those used to generate AVO. To synthesize AB6, the prepared BWO particles (7.8503 g) were added to the solution of AVO precursors to obtain an AVO/BWO molar ratio of 1/3. The subsequent procedures and conditions that were used to generate AB6 were the same as those used to generate AB1.

2.3. Analyses of surface characteristics

The crystalline structures of the photocatalysts were analyzed using X-ray diffraction (XRD) with Cu-Kα radiation (Bruker D8 SSS, Germany) over a 2θ range of 20°–80°. The accelerating voltage and the applied current were set to 40 kV and 40 mA, respectively. The morphologies and microstructures of the samples were observed using scanning electron microscopy (SEM, JEOL 6330 TF, Japan) and transmission electron microscopy (TEM, JEOL 3010, Japan), respectively. The band gaps were calculated from the diffuse reflectance UV-Vis. spectra of the photocatalysts, obtained using a UV-Vis spectrophotometer (JASCO-V670, Japan). The photoluminescence (PL) spectra were obtained using an excitation wavelength of 400 nm on a Hitachi F-4500 fluorescence spectrophotometer (Japan). N_2 adsorption–desorption isotherms were obtained at 77 K using a Micrometrics ASAP 2020 surface area analyzer (USA). The Brunauer–Emmett–Teller (BET) method was used to calculate the specific surface areas from adsorption data. X-ray photoelectron spectroscopy (XPS) measurements were made at room temperature using a PHI 5000 Versal Probe X-ray photoelectron spectrometer (USA). The binding energies were calibrated against C 1s at 284.6 eV. The leaching of Ag from the photocatalysts was measured after the photocatalytic reaction by inductively coupled plasma optical emission spectrometry (ICP-OES, Perkin-Elmer OPTIMA 5300DV, USA). The concentrations of RR2 were evaluated by measuring the absorbance of solutions at a wavelength of 538 nm using a UV-vis spectrophotometer (Hitachi U5100, Japan).

2.4. Experiments to evaluate photo-activity

The photocatalyst dosage, RR2 concentration and temperature in all of the experiments to evaluate photo-activity were 0.5 g/L, 20 mg/L and 298 K, respectively. The solution pH was 3 in all experiments except those conducted to determine the effects of pH. Photocatalysis experiments were performed in a 3 L glass reactor. A 400 W Xe lamp (200 nm < wavelength < 700 nm, UniVex BT-580, Taiwan) was used to provide ultraviolent (UV) radiation with an intensity of 30.3 mW/cm^2. The light source was a xenon lamp. A quartz plate that was filled with 2 M $NaNO_2$ solution was placed on top of the reactor to cut the UV and to provide visible light [21]. Adsorption experiments were conducted in darkness. To detect the active species that were responsible for the photocatalytic reactivity, trapping experiments were performed. In a process similar to that used in the photocatalysis experiment, scavengers K_2CrO_4, EDTA-2Na and IPA were introduced into the RR2 solution before the photocatalyst was added; these were scavengers of superoxide anion radicals ($O_2^{-\bullet}$) [22], h^+ [6,23] and hydroxyl radicals ($HO^\bullet$) [6,23], respectively. The reaction medium was stirred continuously at 300 rpm and aerated with air to maintain a suspension. Following sampling at known intervals, solids were separated by filtration through a 0.22 μm filter (Millipore, USA). To examine the stability and reusability of BA3, three cycles of photodegradation on RR2 were conducted. After each run, the photocatalyst was recycled after washing and drying at 333 K for 24 h for use in the subsequent run. The photocatalytic experiments were performed in triplicate and mean values were reported.

3. Results and discussion

3.1. Determinations of surface properties of photocatalysts

The structures of the crystal phases of the photocatalysts were determined using XRD, and the results are shown in Fig. 1. For AVO, 2θ values of 30.8° and 32.3° correspond to the lattice planes of (–1 2 1) and (1 2 1), respectively. The observed pattern indicates that the prepared AVO has a monoclinic structure, corresponding to the JCPDS standard of 43-0542, and no trace of any other phase is detected. The diffraction peaks with 2θ values of 28.3°, 32.7°, 47.1° and 56.0° correspond to the (1 3 1), (0 6 0), (2 0 2) and (1 3 3) planes of the BWO orthorhombic crystalline phase (JCPDS 39-0256). For AB1–AB4, the intensities of the diffraction peak at 30.8° from AVO decreases as the mole fraction of AVO decreases. All of the peaks from AVO/BWO composites are assigned to AVO or BWO, and no other peak is observed, revealing that AVO and BWO were successfully composited. Additionally, the diffraction peaks of BWO and AB6 had the same 2θ values. For AB1–AB5, only AVO was identified from the XRD patterns; moreover, for AB6, only BWO was identified. The synthesis temperatures of AVO, BWO and AVO/BWO composites were 393, 433 and 393 K, respectively. The BWO in AB1–AB5 might have retained an amorphous,

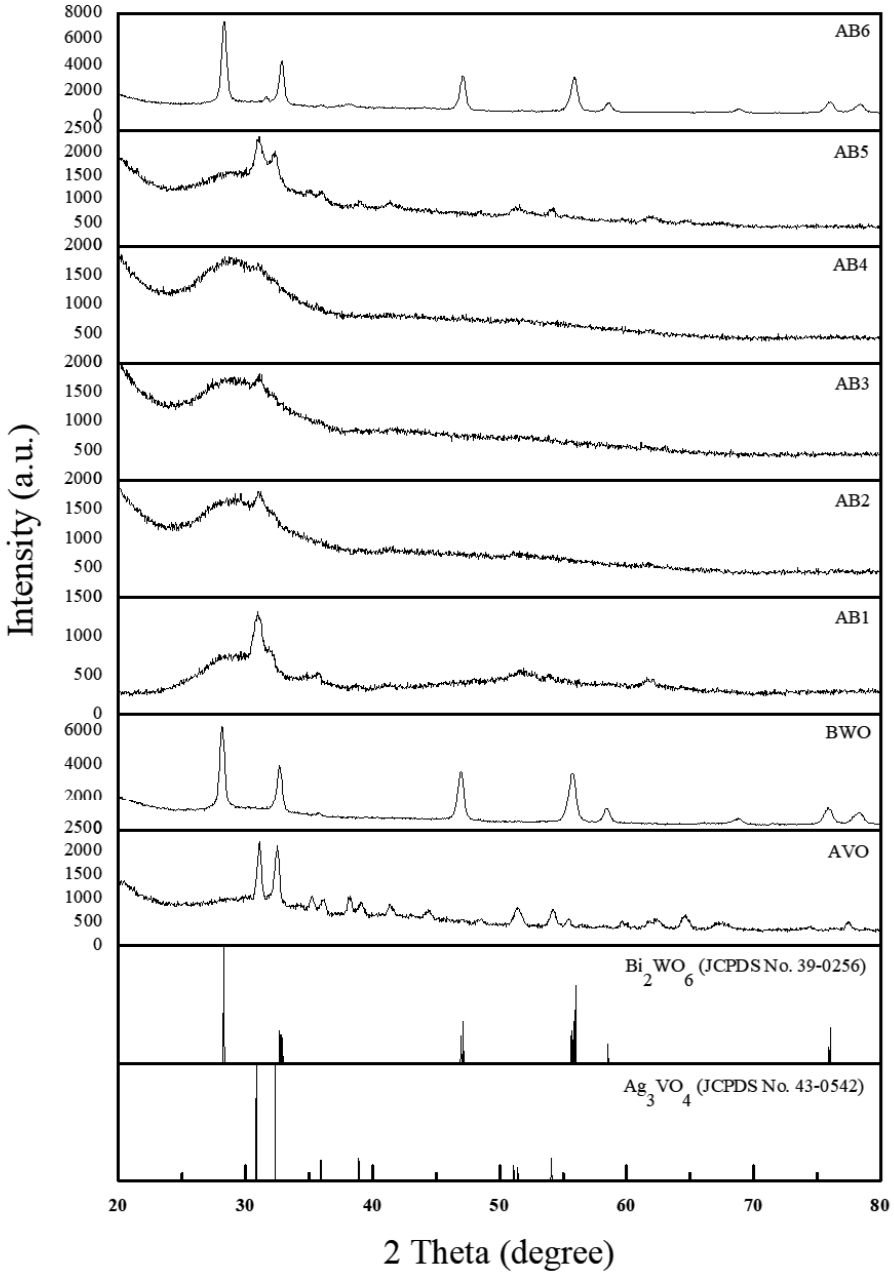

Fig. 1. XRD patterns of synthesized photocatalysts.

poorly crystallized structure under 393 K. Hence, BWO was not identified in AB1–AB5. AB6 was synthesized by a two-step hydrothermal method. BWO solids were firstly generated by a hydrothermal method and then the precursors of AVO were added to synthesize AB6, also by a hydrothermal method. Since the molar ratio of AVO/BWO was 1/3; hence, only BWO was identified in AB6.

Fig. 2 presents the surface morphologies of the synthesized photocatalysts, imaged using SEM. The AVO (Fig. 2a) comprised mainly irregular particles, while the BWO (Fig. 2b) and AB6 (Fig. 2h) exhibited thin flat crystals. AB1–AB5 (Fig. 2c–g) all comprised sponge-like microspheres that were formed by the aggregations of irregular particles and thin flat crystals. All synthesized photocatalysts exhibited significant agglomeration. Fig. 3a–d show the TEM images of AVO, BWO, AB3 and AB6, respectively. AVO particles had average diameters of 50–150 nm (Fig. 3a) and BWO flat crystals had a mean width of 50–100 nm (Fig. 3b). Fig. 3c and d show that irregular AVO particles and BWO flats mixed with each other and formed good interfaces. These results show that the AB3 and AB6 nanocomposites had good crystalline structures with numerous AVO nanoparticles distributed on top of BWO nanoplates.

The equation $E_g = 1{,}240/\lambda$ relates the band gap E_g (eV) to the incident wavelength λ (nm). The band gaps of AVO, BWO, AB1, AB2, AB3, AB4, AB5 and AB6 were

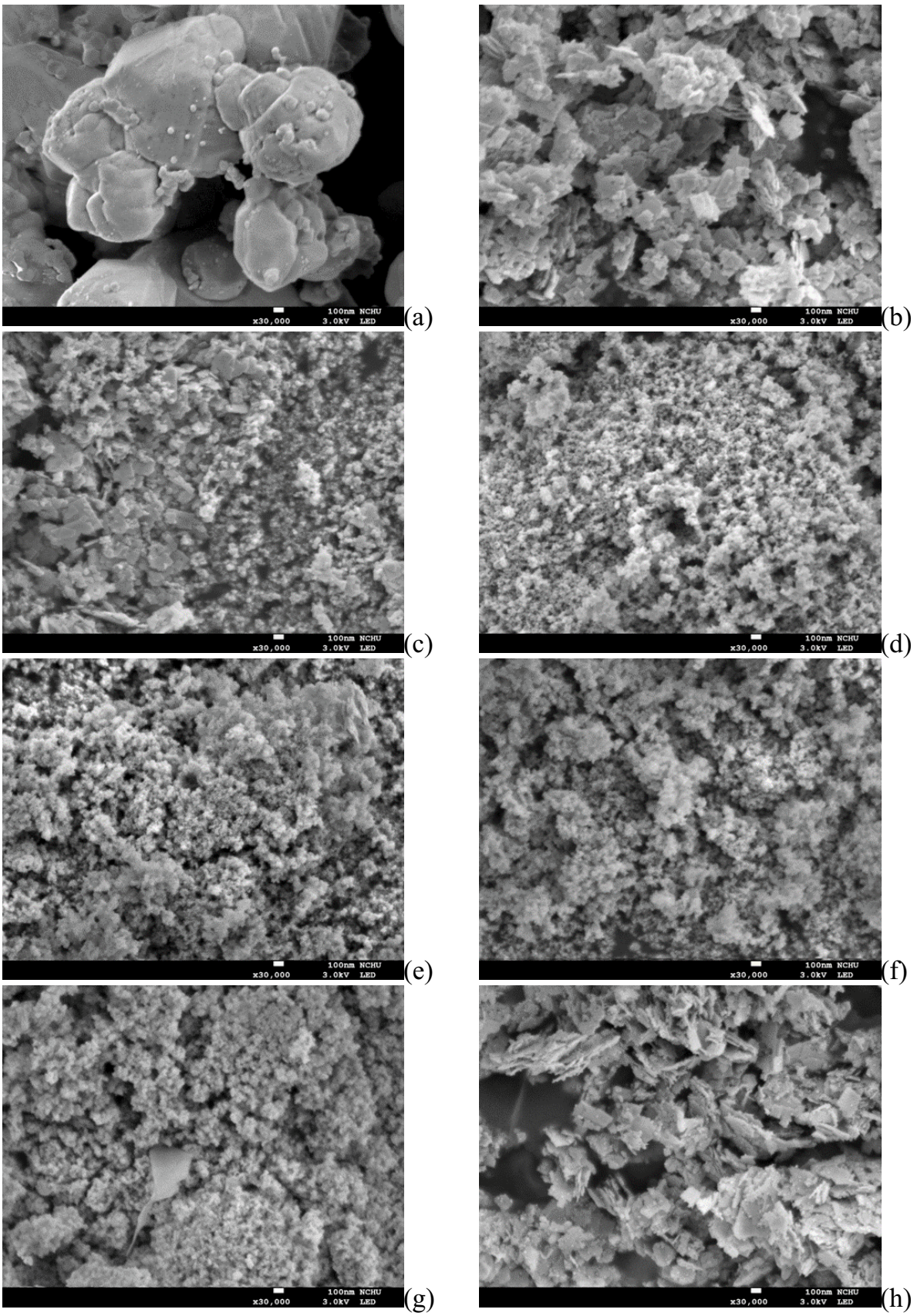

Fig. 2. SEM image of photocatalyst (a) AVO, (b) BWO, (c) AB1, (d) AB2, (e) AB3, (f) AB4, (g) AB5, and (h) AB6.

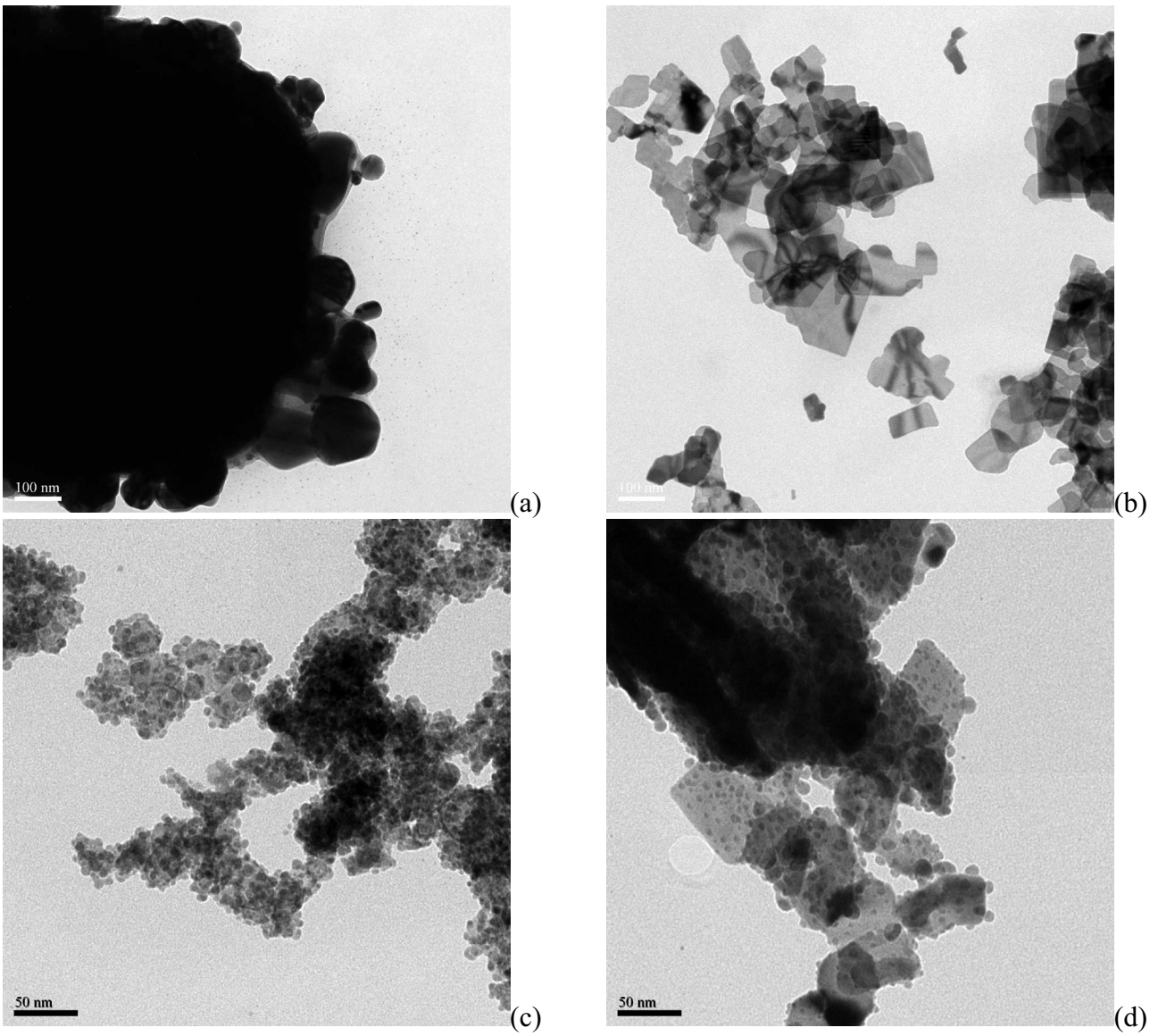

Fig. 3. TEM image of photocatalyst (a) AVO, (b) BWO, (c) AB3, and (d) AB6.

thus estimated to be 1.5, 2.8, 1.7, 1.9, 2.0, 2.0, 1.7 and 2.7 eV, respectively (Table 1). The band gap energies of AVO/BWO composites slightly exceeded that of AVO and were lower than that of BWO. The BET surface areas of AVO, BWO, AB1, AB2, AB3, AB4, AB5 and AB6 were 0.056, 12.93, 37.83, 35.78, 36.68, 39.64, 28.69 and 13.68 m^2/g, respectively (Table 1). The combination of BWO nanosheets and AVO nanoparticles considerably increased the BET surface area. The increase in BET surface area increased the adsorption of organic pollutants, favoring further photocatalytic degradation.

Fig. 4a plots the N_2 adsorption–desorption curve of AB3. Chen et al. [24] indicated that a type I N_2 adsorption–desorption curve, suggesting that the photocatalyst is a typical microporous material. AB3 exhibited a type III isotherm, consistent with a non-porous or macroporous solid material (Fig. 4a). The deviation of the curve from the X-axis at low pressure indicated that the force between nitrogen and AB3 was weak [25]. AB3 exhibited type III N_2 adsorption–desorption hysteresis loops of H_3, which is considered to be associated with the slit pores that were formed by the accumulation of flake particles [26]. Fig. 4b shows the pore diameter distribution of AB3; the pore size AB3 was approximately 90 nm. This study suggests that AB3 is expressed as a macroporous material, owing to its sponge-like structure.

PL spectra are widely used to elucidate the migration, transfer and recombination processes of photo-generated electron–hole pairs in photocatalysts. Fig. 5 shows the PL spectra of all synthesized photocatalysts. A higher intensity of PL corresponds to a greater probability of recombination of electron–hole pair becomes. All of the samples exhibited a strong emission peak that was centered at approximately 430 nm. BWO yielded the highest peak intensity, while AVO

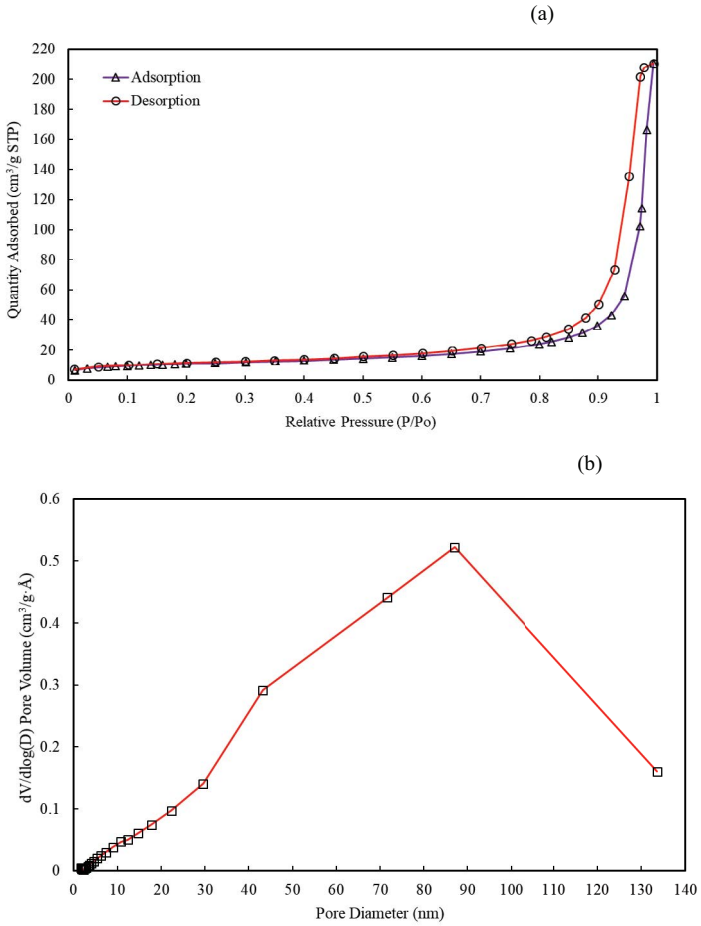

Fig. 4. BET measurement of AB3 (a) N_2 adsorption–desorption isotherms and (b) pore diameter distribution curves.

Table 1
Surface characteristics and pseudo-first-order rate constants of photocatalysts ([RR2] = 20 mg/L, [photocatalyst] = 0.5 g/L, pH = 3)

Photocatalysts	BET (m^2/g)	Band gap (eV)	k (min^{-1})	R^2
AVO	0.056	1.5	0.0066	0.959
			(0.0229)[a]	(0.998)[a]
BWO	12.93	2.8	0.0053	0.809
AB1	37.83	1.7	0.0188	0.962
AB2	35.78	1.9	0.0425	0.998
AB3	36.68	2.0	0.0894	0.998
			(0.1355)[a]	(0.976)[a]
			(0.0103)[b]	(0.931)[b]
AB4	39.64	2.0	0.0666	0.995
AB5	28.69	1.7	0.0106	0.968
AB6	13.68	2.7	0.0162	0.981

()[a]: solar irradiation at pH 3;
()[b]: at pH 11.

yielded a slightly lower peak intensity. AB1–AB5 had lower peak intensities than AVO and BWO (Fig. 5), indicating that the formation of AVO/BWO composite inhibited the recombination of photo-excited e^- and h^+.

The valance and surface chemical compositions of AB3 were examined using XPS, and the results are shown in Fig. 6. Ag $3d_{5/2}$ and Ag $3d_{3/2}$ peaks appeared at 367 and 373 eV, respectively (Fig. 6a), confirming that the Ag species

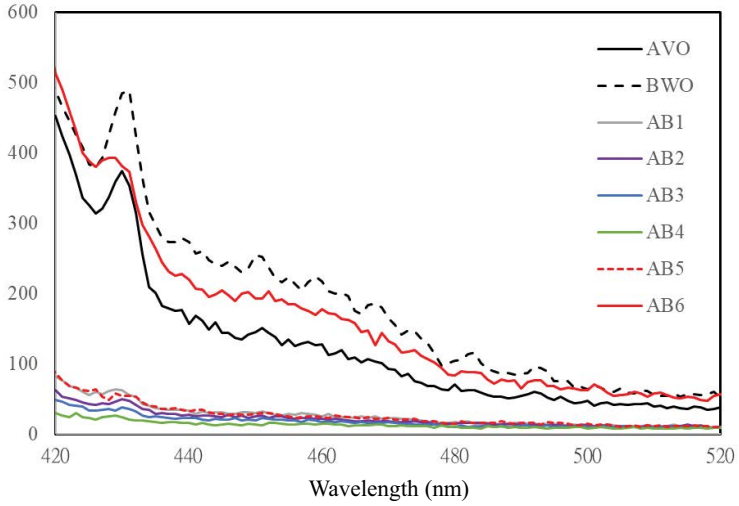

Fig. 5. PL spectra of synthesized photocatalysts.

was Ag^+ [13–15,18,27]. The Bi $4f_{5/2}$ and Bi $4f_{7/2}$ peaks at 163.3 and 157.9 eV, respectively (Fig. 6b), were consistent with Bi^{3+} [18,28–30]. The W $4f_{5/2}$ and W $4f_{7/2}$ peaks at 36.1 and 34.0 eV, respectively (Fig. 6c), revealed the presence of W^{6+} [13,31]. Fig. 6d shows the V $2p_{1/2}$ and V $2p_{3/2}$ peaks at 522 and 515.3 eV, respectively, confirming that V was present as V^{5+} [16,18,32]. The O 1s peaks at 528.9, 529.0, 530.0, 530.6 and 531.9 eV correspond to Ag–O [33], Bi–O [34], V–O [35], W–O [6] and –OH [35–37] bonds (Fig. 6e). The theoretical atomic molar ratio of Ag–O/Bi–O in AB3 is 1:2. The Ag–O/Bi–O area ratio of AB3 was determined by quantitative analysis to be 1:2.01 (Fig. 6e), which is almost the same as the dose of BWO that was added to AVO.

3.2. Evaluation of photo-activity of synthesized photocatalysts

The photo-activity of the prepared samples was evaluated by the removal of RR2 aqueous solution under Vis. irradiation. Fig. 7 plots the concentrations of RR2 that were removed using all prepared photocatalysts. The efficiencies of removal of RR2 after 60 min of adsorption by all photocatalysts were all less than 16% (Fig. 7a). RR2 was not effectively removed by adsorption. The removal efficiencies of RR2 after 20 min of Vis. irradiation using AB1, AB2, AB3, AB4, AB5 and AB6 were 36%, 58%, 82%, 72%, 24% and 32%, respectively, which were much higher than those obtained using pristine AVO (17%) and BWO (12%) (Fig. 7b). Evidently, the highest RR2 removal percentage was found at AVO/BWO = 1/3. To compare the photocatalytic degradation efficiencies of the photocatalysts, their kinetic behaviors in RR2 photodegradation were investigated. The photodegradation of RR2 closely fitted the following pseudo-first-order equation [Eq. (1)] [8,9,17,20].

$$\ln\left(\frac{C_0}{C}\right) = k_t \tag{1}$$

where C_0 and C represent the initial and residual concentrations of RR2 solution; t is the reaction time (min), and k is the reaction rate constant (min^{-1}).

A highly linear relationship was observed between $\ln(C_0/C)$ and irradiation time (Table 1). The k values of all AVO/BWO composites greatly exceeded those of AVO (0.0066 min^{-1}) and BWO (0.0053 min^{-1}). The k values followed the trend AB3 > AB4 > AB2 > AB1 > AB6 > AB5 (Table 1). AB3 exhibited the best performance. Apparently, the introduction of too little or too much BWO did not contribute to the efficient separation of charge carriers, resulting in an unsatisfactory activity, as in previous studies [12]. Hu and Hu [38] and Chen et al. [39] suggested that when the amount of dopant exceeds its optimal value, it may provide recombination centers for the photo-generated e^- and h^+, reducing the thickness of the space-charge layer on the surface of each photocatalyst particle, and thereby reducing the absorption of photons.

The photocatalytic performance of photocatalysts is affected by the following factors; surface area (adsorption activity), crystal phase, electronic properties (including band gap, band edge potential and charge carrier mobility), and others. The AVO/BWO composites exhibit much greater activity than pure AVO and BWO in the degradation of RR2 under Vis. irradiation. The first reason for this finding was that the greater surface area of AVO/BWO composites induced the adsorption of a higher percentage of RR2 molecules, inducing higher photo-activity because the local concentration of RR2 on the surface of the AVO/BWO composites was higher. The second reason was the formation of heterojunctions between AVO and BWO. The photo-generated charges can be transferred through the formed heterojunctions much more quickly. Therefore, the recombination rate of photo-generated electron–hole pairs was reduced, and more radicals formed, favoring the degradation of RR2. Li et al. [12] and Zhang and Ma [13] also suggested that the enhanced photo-activity is attributable to the formation of AVO/BWO heterojunctions, which facilitate the separation and migration of photo-generated carriers.

Fig. 8 plots the effects of pH and solar irradiation on the removal of RR2 by AVO and AB3. After 20 min reaction, the RR2 removal percentages at pH 3 and pH 11 for AVO under

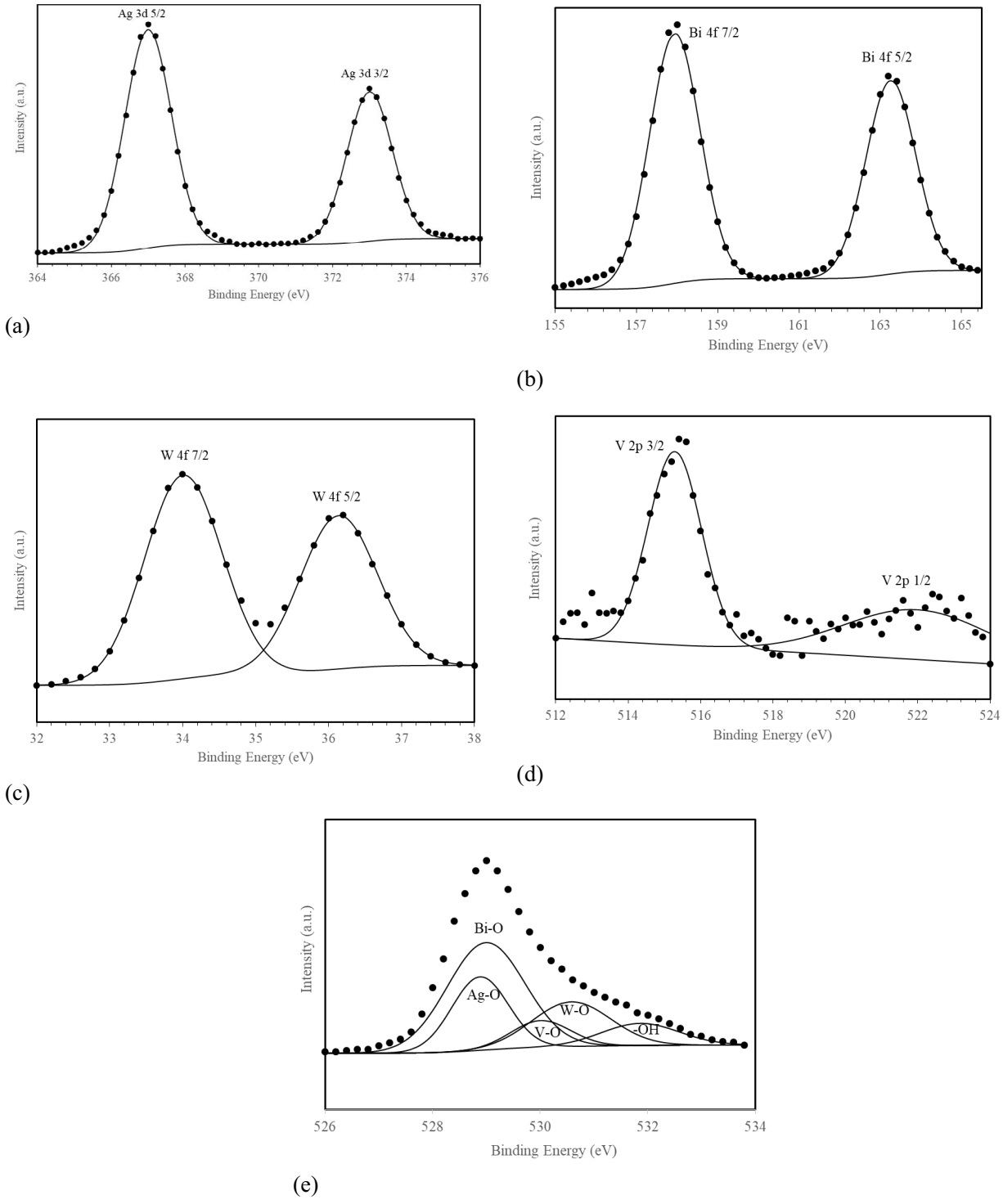

Fig. 6. XPS spectra of AB3 (a) Ag 3d, (b) Bi 4f, (c) W 4f, (d) V 2p, and (d) O 1s.

Vis. irradiation were 17% and 7%, respectively, whereas those for AB3 were 82% and 25%, respectively. The RR2 photodegradation performance at pH 3 exceeded that at pH 11 owing to the change in electrostatic attraction or repulsion between RR2 and AB3. RR2 is an anionic dye so the electrostatic attraction between RR2 molecules and AB3 was much greater at pH 3. Furthermore, at a high pH value, the negatively charged AB3 surface prevented the sorption of hydroxide ions, reducing the formation of $HO^{\bullet}$ and the photo-activity. At pH 3, the k values of AVO and AB3 under solar irradiation were 0.0229 and 0.1355 min^{-1}, respectively, which were about 3.47 and 1.52 times those under Vis. irradiation, respectively.

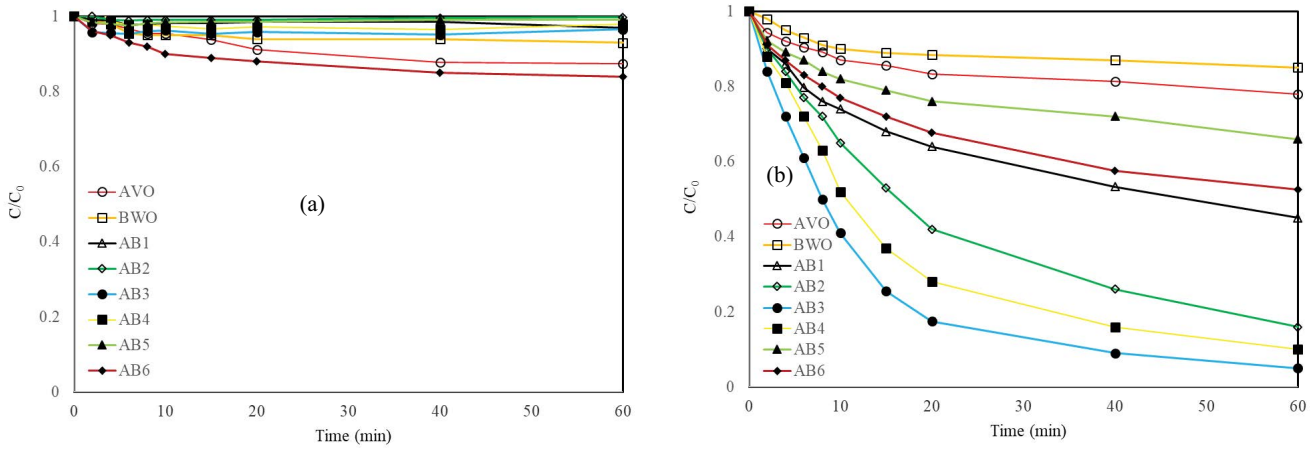

Fig. 7. Comparisons of removal of RR2 by all photocatalysts (a) adsorption and (b) Vis. photocatalysis ([RR2] = 20 mg/L, pH = 3, [photocatalyst] = 0.5 g/L).

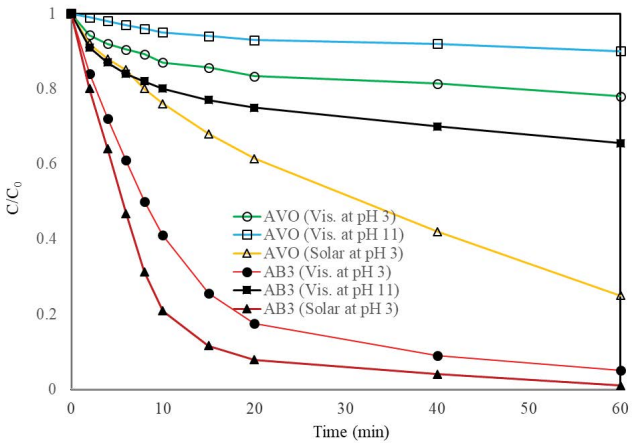

Fig. 8. Effects of pH and solar irradiation on RR2 removal by AVO and AB3 ([RR2] = 20 mg/L, [photocatalyst] = 0.5 g/L).

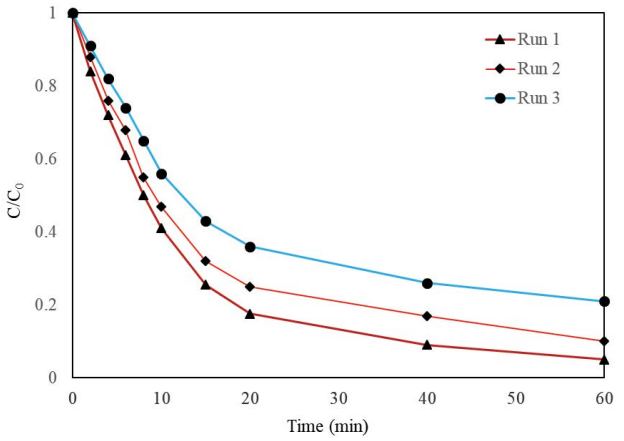

Fig. 9. Comparisons of cyclic photodegradation of RR2 in Vis./AB3 system ([RR2] = 20 mg/L, pH = 3, [AB3] = 0.5 g/L).

AB3 was found herein to be effectively photo-excited by solar irradiation to degrade RR2.

From a practical perspective, photocatalytic materials with good stability are essential. To evaluate their stability, a recycling test of RR2 photodegradation over AB3 was performed. After 60 min Vis. irradiation, the removal percentages of RR2 by AB3 in the first, second and third runs were 95%, 90% and 79%, respectively (Fig. 9). The AB3 was examined before and after RR2 photodegradation using the XRD technique to observe its structural change. Fig. 10 plots the XRD patterns of fresh and used AB3. Some changes in the positions and intensities of the diffraction peaks between the fresh and used AB3 are observed. The phase composition of AB3 after the photocatalytic experiment remains largely unchanged from that before the experiment, except for the formation of a little Ag. The Ag^+ in the Ag-based photocatalysts is easily reduced by photo-generated e^- under light irradiation [40]. A peak at 38.1° ((1 1 1) plane of Ag (JCPDS 65-2871)) was obtained from the used AB3 (Fig. 10). Additionally, the intensity of the signal from the (1 1 1) plane of Ag increased with the number of uses. After 60 min of Vis. irradiation, the concentrations of Ag^+ that had leached from AB3 after runs 1, 2 and 3 were 11.7, 0.212 and 0.176 mg/L, which were lower than those of that leached from AVO (194 mg/L). Hence, the photocatalytic stability of AB3 exceeded that of AVO. The Ag^+ ions that leached from AB3 composite were reduced to metallic Ag on the surface of the used AB3. Consequently, the photo-corrosion of the photocatalyst might have been responsible for the slight decline in photo-activity [13,40]. Dai et al. [41] indicated that the silver ions (Ag^+) of AVO are gradually reduced to silver (Ag) during photocatalytic degradation. Excessive Ag blocks the active sites of AVO, reducing its photocatalytic performance.

Fig. 11 presents the results of radical-capture experiments. When IPA (scavenger of $HO^•$) was used, the RR2 removal percentage was 90% after 60 min of reaction, which is close to that (95%) achieved without a scavenger, indicating

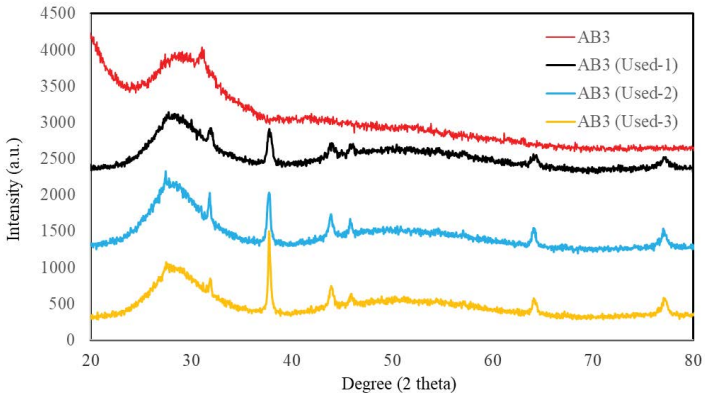

Fig. 10. XRD patterns of used AB3.

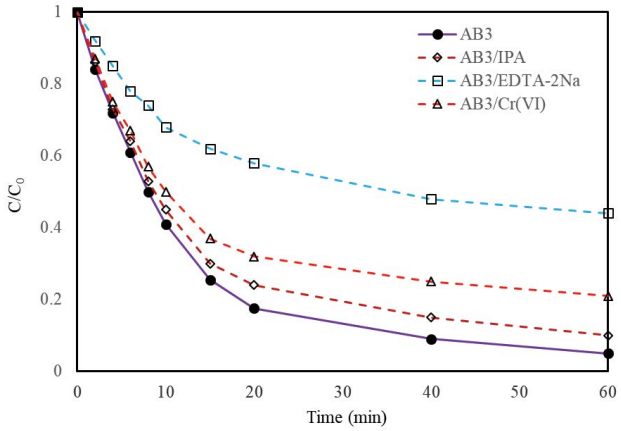

Fig. 11. Photocatalysis of RR2 in presence of scavengers for Vis./AB3 system ([RR2] = 20 mg/L, pH = 3, [AB3] = 0.5 g/L).

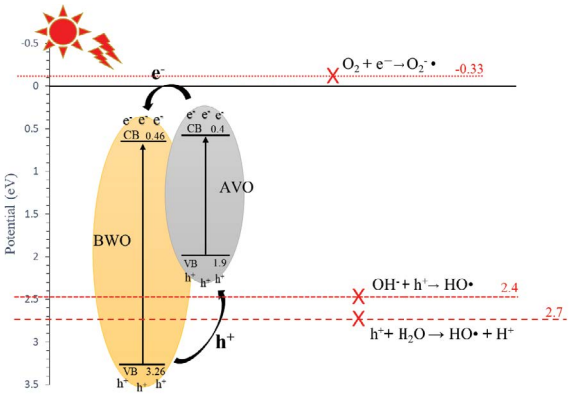

Fig. 12. Energy band diagram and possible charge-separation process of Vis./AB3 system.

that HO• is not involved in the photodegradation of RR2. However, adding EDTA-2Na (scavenger of h^+) or Cr(VI) (scavenger of $O_2^{\bullet-}$) markedly reduced the RR2 removal percentage to 56% or 79%, respectively. The effect of EDTA-2Na exceeds those of other scavengers, suggesting that h^+ is the main active species. Hence the contribution of the reactive species follows the order $h^+ > O_2^{\bullet-} >$ HO•. Li et al. [12] and Zhang and Ma [13] found that h^+ and $O_2^{\bullet-}$ had critical roles in the photocatalytic process of AVO/BWO composites.

3.3. Mechanism of enhanced photo-activity in AB3 heterojunction

The efficient separation of photo-generated electron–hole pairs is well known to be important in photocatalysis. The VB and CB edge potentials of each photocatalyst at the point of zero charge were calculated using Eqs. (2) and (3) [42–45]:

$$E_{CB} = X - E_e - 0.5E_g \quad (2)$$

$$E_{VB} = E_{CB} + E_g \quad (3)$$

where X is the absolute electronegativity of the photocatalyst, given by the geometric mean of the absolute electronegativities of the constituent atoms. The absolute electronegativity is defined as the arithmetic mean of the atomic electron affinity and the first ionization energy. The X values for AVO and BWO are 5.65 [12] and 6.36 eV [46], respectively. E_e is the energy of free electrons on the hydrogen scale (4.5 eV) and E_{CB} and E_{VB} are the CB and VB edge potentials, respectively [44]. The E_{CB} values of AVO and BWO are determined to be 0.40 and 0.46 eV, respectively, relative to the NHE level. The E_{VB} values of AVO and BWO are determined to be 1.90 and 3.26 eV, respectively. Under Vis. irradiation, both AVO and BWO absorb Vis. photons to generate photo-generated e^- in the CB and h^+ in the VB. The difference between CB and VB potentials establishes a potential difference across the interface of the two photocatalysts, forming a heterojunction. Fig. 12 shows the energy band diagram and possible charge-separation process of AB3. Photo-excited e^- flowed from the CB of AVO to BWO owing to its more positive potential (0.46 eV). Meanwhile, h^+ flowed from the VB of BWO to AVO. Therefore, the useful e^- in the CB of BWO and the h^+ in the VB of AVO were all used. Hence, the recombination of the photo-generated electron–hole pairs was effectively inhibited; their lifetimes were prolonged, and so

the photo-activity of the AB3 heterojunction was greatly improved. The CB edge potential of BWO was more positive than that of $O_2/O_2^{\bullet}$ (–0.33 V/NHE) [32]; therefore, the photo-induced e^- may not be trapped by the absorbed O_2, generating $O_2^{\bullet}$. Since the potentials of $HO^{\bullet}/OH^-$ (2.4 eV, vs. NHE) [47] and $HO^{\bullet}/H_2O$ (2.7 eV, vs. NHE) [32] are more positive than the VB of AVO (1.9 eV, vs. NHE), the h^+ on the VB of AVO cannot react with OH^- and H_2O to form $HO^{\bullet}$ and directly participate in the photodegradation of RR2. The AB3 more efficiently generated photo-generated electron–hole pairs and promoted the separation of photo-generated electron–hole pairs owing to the synergy of the AVO and BWO.

4. Conclusions

In the present investigation, the hydrothermal method was used to prepare a series of AVO/BWO composites with various AVO/BWO molar ratios, which were characterized using XRD, SEM, TEM, UV-Vis., BET, PL, and XPS techniques. Among the prepared composites, the AVO/BWO composite with the AVO/BWO molar ratio of 1/3 exhibited the best photo-activity and an excessive amount of AVO reduced photo-activity. The RR2 photodegradation rate constants in Vis./AB3 and solar/AB3 systems were 0.0894 and 0.1355 min^{-1}, respectively. The AB3 heterojunction exhibited remarkably greater photo-activity than pure AVO and BWO owing to its higher light harvesting efficiency and the induction of efficient photo-generated electron–hole separation by the suitably matching conduction and valence band levels of AVO and BWO. The recycling experiments revealed that AB3 had reasonable stability. The experimental results revealed that h^+ was the major active species of AB3 in the photodegradation of RR2.

Acknowledgements

The authors would like to thank the Ministry of Science and Technology for financially supporting this research under Contract No. 110-2221-E-992-026-MY2.

References

[1] Z. Zhu, R. Rao, Z. Zhao, J. Chen, W. Jiang, F. Bi, Y. Yang, X. Zhang, Research progress on removal of phthalates pollutants from environment, J. Mol. Liq., 355 (2022) 118930, doi: 10.1016/j.molliq.2022.118930.

[2] N. Lin, Y. Gong, R. Wang, Y. Wang, X. Zhang, Critical review of perovskite-based materials in advanced oxidation system for wastewater treatment: design, applications and mechanisms, J. Hazard. Mater., 424 (2022) 127637, doi: 10.1016/j.jhazmat.2021.127637.

[3] N. Liu, W. Dai, F. Fei, H. Xu, J. Lei, G. Quan, Y. Zheng, X. Zhang, L. Tang, Insights into the photocatalytic activation persulfate by visible light over ReS_2/MIL-88B(Fe) for highly efficient degradation of ibuprofen: combination of experimental and theoretical study, Sep. Purif. Technol., 297 (2022) 121545, doi: 10.1016/j.seppur.2022.121545.

[4] Y. Yang, X. Li, B. Jie, Z. Zheng, J. Li, C. Zhu, S. Wang, J. Xu, X. Zhang, Electron structure modulation and bicarbonate surrounding enhance Fenton-like reactions performance of Co-Co PBA, J. Hazard. Mater., 437 (2022) 129372, doi: 10.1016/j.jhazmat.2022.129372.

[5] R. Konta, H. Kato, H. Kobayashi, A. Kudo, Photophysical properties and photocatalytic activities under visible light irradiation of silver vanadates, Phys. Chem. Chem. Phys., 5 (2003) 3061–3065.

[6] M.S. Gui, W.D. Zhang, Q.X. Su, C.H Chen, Preparation and visible light photocatalytic activity of Bi_2O_3/Bi_2WO_6 heterojunction photocatalysts, J. Solid State Chem., 184 (2011) 1977–1982.

[7] W. He, Y. Sun, G. Jiang, H. Huang, X. Zhang, F. Dong, Activation of amorphous Bi_2WO_6 with synchronous Bi metal and Bi_2O_3 coupling: photocatalysis mechanism and reaction pathway, Appl. Catal., B, 232 (2018) 340–347.

[8] C.H. Wu, C.Y. Kuo, C.D. Dong, C.W. Chen, Y.L. Lin, W.J. Huang, Single-step solvothermal process for synthesizing SnO_2/Bi_2WO_6 composites with high photocatalytic activity in the photodegradation of C.I. Reactive Red 2 under solar light, React. Kinet. Mech. Catal., 126 (2019) 1097–1113.

[9] C.H. Wu, C.D. Dong, C.W. Chen, Y.L. Lin, S.R. Jhu, Y.H. Lin, Enhanced visible light photocatalysis of $Bi_2O_3/BiVO_4$ and Bi_2O_3/Ag_3VO_4 heterojunction: effects of synthetic procedures, Desal. Water Treat., 209 (2021) 267–279.

[10] H. Fang, Y. Pan, H. Yan, L. Xu, C. Pan, Surface deposition of Ag/Ag_3VO_4 on rod-like $BiPO_4$ to construct plasmon-induced heterostructures with ameliorated photocatalytic performance, Mater. Sci. Semicond. Process., 127 (2021) 105722, doi: 10.1016/j.mssp.2021.105722.

[11] P. Wang, H. Tang, Y. Ao, C. Wang, J. Hou, J. Qian, Y. Li, In-situ growth of Ag_3VO_4 nanoparticles onto BiOCl nanosheet to form a heterojunction photocatalyst with enhanced performance under visible light irradiation, J. Alloys Compd., 688 (2016) 1–7.

[12] S. Li, S. Hu, W. Jiang, Y. Liu, J. Liu, Z. Wang, Facile synthesis of flower-like Ag_3VO_4/Bi_2WO_6 heterojunction with enhanced visible light photocatalytic activity, J. Colloid Interface Sci., 501 (2017) 156–163.

[13] J. Zhang, Z. Ma, Enhanced visible light photocatalytic performance of Ag_3VO_4/Bi_2WO_6 heterojunctions in removing aqueous dyes and tetracycline hydrochloride, J. Taiwan Inst. Chem. Eng., 78 (2017) 212–218.

[14] J. Zhang, Z. Ma, Flower-like Ag_3VO_4/BiOBr n-p heterojunction photocatalysts with enhanced visible light-driven catalytic activity, Mol. Catal., 436 (2017) 190–198.

[15] S. Wang, Y. Guan, L. Wang, W. Zhao, H. He, J. Xiao, S. Yang, C. Sun, Fabrication of a novel bifunctional material of BiOI/Ag_3VO_4 with high adsorption-photocatalysis for efficient treatment of dye wastewater, Appl. Catal., B, 168–169 (2015) 448–457.

[16] J. Zhang, Z. Ma, $Ag_3VO_4/BiOIO_3$ heterojunction with enhanced visible light-driven catalytic activity, J. Taiwan Inst. Chem. Eng., 88 (2018) 177–185.

[17] C.H. Wu, C.Y. Kuo, C.D. Dong, C.W. Chen, Y.L. Lin, Y.S. Kuan, Synthesis, characterization and photocatalytic activity of a novel Bi_2O_3/Ag_3VO_4 heterojunction photocatalyst, Desal. Water Treat., 198 (2020) 364–375.

[18] W. Zhao, Y. Feng, H. Huang, P. Zhou, J. Li, L. Zhang, B. Dai, J. Xu, F. Zhu, N. Sheng, D.Y.C. Leung, A novel z-scheme $Ag_3VO_4/BiVO_4$ heterojunction photocatalyst: study on the excellent photocatalytic performance and photocatalytic mechanism, Appl. Catal., B, 245 (2019) 448–458.

[19] L. Liu, T. Hu, K. Dai, J. Zhang, C. Liang, A novel step-scheme $BiVO_4/Ag_3VO_4$ photocatalyst for enhanced photocatalytic degradation activity under visible light irradiation, Chin. J. Catal., 42 (2021) 46–55.

[20] C.H. Wu, C.D. Dong, C.W. Chen, Y.L. Lin, Y.R. Cheng, G.Y. Lee, Synthesis of novel $Bi_2O_3/BiVO_4/Ag_3VO_4$ heterojunction photocatalyst with enhanced photocatalytic activity under visible light irradiation, Desal. Water Treat., 228 (2021) 351–361.

[21] M. Su, C. He, V.K. Sharma, M.A. Asi, D. Xia, X.Z. Li, H. Deng, Y. Xiong, Mesoporous zinc ferrite: synthesis, characterization, and photocatalytic activity with H_2O_2/visible light, J. Hazard. Mater., 211–212 (2012) 95–103.

[22] Y. Chen, S. Yang, K. Wang, L. Lou, Role of primary active species and TiO_2 surface characteristic in UV-illuminated photodegradation of Acid Orange 7, J. Photochem. Photobiol., A, 172 (2005) 47–54.

[23] H. Huang, K. Liu, K. Chen, Y. Zhang, Y. Zhang, S. Wang, Ce and F comodification on the crystal structure and enhanced photocatalytic activity of Bi_2WO_6 photocatalyst under visible light irradiation, J. Phys. Chem. C, 118 (2014) 14379–14387.
[24] J. Chen, Y. Yang, S. Zhao, F. Bi, L. Song, N. Liu, J. Xu, Y. Wang, X. Zhang, Stable black phosphorus encapsulation in porous mesh-like UiO-66 promoted charge transfer for photocatalytic oxidation of toluene and o-dichlorobenzene: performance, degradation pathway, and mechanism, ACS Catal., 12 (2022) 8069–8081.
[25] P.A. Webb, C. Orr, Analytical Methods in Fine Particle Technology, Micromeritics Instrument Corp, Norcross, 1997.
[26] M. Thommes, In: G.Q. Lu, X.S. Zhao, Eds., Nanoporous Materials: Science and Engineering, Imperial College Press, London, 2004, p. 317.
[27] Y. Wang, F. Bi, Y. Wang, M. Jia, X. Tao, Y. Jin, X. Zhang, MOF-derived CeO_2 supported Ag catalysts for toluene oxidation: the effect of synthesis method, Mol. Catal., 515 (2021) 111922, doi: 10.1016/j.mcat.2021.111922.
[28] H. Li, Y. Sun, B. Cai, S. Gan, D. Han, L. Niu, T. Wu, Hierarchically Z-scheme photocatalyst of Ag@AgCl decorated on $BiVO_4$ (0 4 0) with enhancing photoelectrochemical and photocatalytic performance, Appl. Catal., B, 170–171 (2015) 206–214.
[29] J. Sun, X. Li, Q. Zhao, M.O. Tade, S. Liu, Construction of p-n heterojunction β-Bi_2O_3/$BiVO_4$ nanocomposite with improved photoinduced charge transfer property and enhanced activity in degradation of *ortho*-dichlorobenzene, Appl. Catal., B, 219 (2017) 259–268.
[30] Y. Yang, W. Ji, X. Li, Z. Zheng, F. Bi, M. Yang, J. Xu, X. Zhang, Insights into the degradation mechanism of perfluorooctanoic acid under visible light irradiation through fabricating flower-shaped Bi_5O_7I/ZnO n-n heterojunction microspheres, Chem. Eng. J., 420 (2021) 129934, doi: 10.1016/j.cej.2021.129934.
[31] D. Ma, J. Wu, M. Gao, Y. Xin, T. Ma, Y. Sun, Fabrication of Z-scheme g-C_3N_4/RGO/Bi_2WO_6 photocatalyst with enhanced visible light photocatalytic activity, Chem. Eng. J., 290 (2016) 136–146.
[32] Y. Xie, Y. Dai, X. Yuan, L. Jiang, L. Zhou, Z. Wu, J. Zhang, H. Wang, T. Xiong, Insight on the plasmonic Z-scheme mechanism underlying the highly efficient photocatalytic activity of silver molybdate/silver vanadate composite in rhodamine B degradation, J. Colloid Interface Sci., 530 (2018) 493–504.
[33] S. Akel, R. Dillert, N.O. Balayeva, R. Boughaled, J. Koch, M. El Azzouzi, D.W. Bahnemann, Ag/Ag_2O as a co-catalyst in TiO_2 photocatalysis: effect of the co-catalyst/photocatalyst mass ratio, Catalysts, 8 (2018) 647, doi: 10.3390/catal8120647.
[34] X. Ma, Z. Ma, T. Liao, X. Liu, Y. Zhang, L. Li, W. Li, B. Hou, Preparation of $BiVO_4$/BiOCl heterojunction photocatalyst by in-situ transformation method for norfloxacin photocatalytic degradation, J. Alloys Compd., 702 (2017) 68–74.
[35] J. Zeng, J. Zhong, J. Li, Z. Xiang, X. Liu, J. Chen, Improvement of photocatalytic activity under solar light of $BiVO_4$ microcrystals synthesized by surfactant-assisted hydrothermal method, Mater. Sci. Semicond. Process., 27 (2014) 41–46.
[36] Q. Chen, Y. Wang, Y. Wang, X. Zhang, D. Duan, C. Fan, Nitrogen-doped carbon quantum dots/Ag_3PO_4 complex photocatalysts with enhanced visible light driven photocatalytic activity and stability, J. Colloid Interface Sci., 491 (2017) 238–245.
[37] Y. Yang, S. Zhao, F. Bi, J. Chen, Y. Wang, L. Cui, J. Xu, X. Zhang, Highly efficient photothermal catalysis of toluene over Co_3O_4/TiO_2 p-n heterojunction: the crucial roles of interface defects and band structure, Appl. Catal., B, 315 (2022) 121550, doi: 10.1016/j.apcatb.2022.121550.
[38] X. Hu, C. Hu, Preparation and visible light photocatalytic activity of Ag_3VO_4 powders, J. Solid State Chem., 180 (2007) 725–732.
[39] S. Chen, W. Zhao, W. Liu, H. Zhang, X. Yu, Y. Chen, Preparation, characterization and activity evaluation of p–n junction photocatalyst p-$CaFe_2O_4$/n-Ag_3VO_4 under visible light irradiation, J. Hazard. Mater., 172 (2009) 1415–1423.
[40] J. Zhang, Z. Ma, Ag-Ag_3VO_4/$AgIO_3$ composites with enhanced visible light-driven catalytic activity, J. Colloid Interface Sci., 524 (2018) 16–24.
[41] K. Dai, L. Lu, J. Dong, Z. Ji, G. Zhu, Q. Liu, Z. Liu, Y. Zhang, D. Li, C. Liang, Facile synthesis of a surface plasmon resonance-enhanced Ag/AgBr heterostructure and its photocatalytic performance with 450 nm LED illumination, Dalton Trans., 42 (2013) 4657–4662.
[42] S. Wang, D. Li, C. Sun, S. Yang, Y. Guan, H. He, Synthesis and characterization of g-C_3N_4/Ag_3VO_4 composites with significantly enhanced visible light photocatalytic activity for triphenylmethane dye degradation, Appl. Catal., B, 144 (2014) 885–892.
[43] X. Meng, Z. Zhang, Bismuth-based photocatalytic semiconductors: Introduction, challenges and possible approaches, J. Mol. Catal. A: Chem., 423 (2016) 533–549.
[44] Q. Shi, W. Zhao, L. Xie, J. Chen, M. Zhang, Y. Li, Enhanced visible light driven photocatalytic mineralization of indoor toluene via a $BiVO_4$/reduced graphene oxide/Bi_2O_3 all-solid-state Z-scheme system, J. Alloys Compd., 662 (2016) 108–117.
[45] L. Jiang, X. Yuan, G. Zeng, J. Liang, X. Chen, H. Yu, H. Wang, Z. Wu, J. Zhang, T. Xiong, In-situ synthesis of direct solid-state dual Z-scheme WO_3/g-C_3N_4/Bi_2O_3 photocatalyst for the degradation of refractory pollutant, Appl. Catal., B, 227 (2018) 376–385.
[46] B. Samran, C. Saranyoo, Highly enhanced photoactivity of $BiFeO_3$/Bi_2WO_6 composite flms under visible light irradiation, Physica B, 575 (2019) 411683, doi: 10.1016/j.physb.2019.411683.
[47] C. Lai, M. Zhang, B. Li, D. Huang, G. Zeng, L. Qin, X. Liu, H. Yi, M. Cheng, L. Li, Z. Chen, L. Chen, Fabrication of CuS/$BiVO_4$ (0 4 0) binary heterojunction photocatalysts with enhanced photocatalytic activity for ciprofloxacin degradation and mechanism insight, Chem. Eng. J., 358 (2019) 891–902.